p-ISSN 2089 – 0133 e-ISSN 2477-6416
URL: https://jurnal.uns.ac.id/ijap/article/view/87634

DOI: https://doi.org/10.13057/ijap.v15i1.87634

THERMO-FLUID DYNAMICS OF PLA DEPOSITION IN FUSED FILAMENT FABRICATION 3D PRINTING: A NUMERICAL STUDY

Zaki Saptari Saldi*, Purba Purnama, Nurmalia Nurmalia, Salman Alfarisi, Muhammad Arifin, Ammar Munadi Suweco
[1]Universitas Pembangunan Jaya, Tangerang, Indonesia
*zaki.saldi@upj.ac.id

Received 05-06-2024, Revised 27-02-2025, Accepted 27-02-2025,
Available Online 01-04-2025, Published Regularly April 2025

ABSTRACT

Prototyping plays an important role in product design and has recently gained benefit from the rising popularity of 3D printing. It is to be expected that 3D printing will accommodate more materials, which need to be tailored to specific design requirements. Insights into heat transfer and fluid flows (thermo-fluid dynamics) in the printing process is thus essential to obtain favorable process parameters that can lead to high quality prints. In this work, polylactic acid (PLA) melt in Fused Filament Fabrication (FFF) 3D printing was numerically studied through Computational Fluid Dynamics (CFD) simulations, with a focus on the thermo-fluid dynamics of the strand deposition of the filament melt on the printer platform. The study was carried out by evaluating 6 printing cases, with a variation of 2 key process parameters, i.e., printing speed (30 and 45 mm/s) and platform temperature (310, 320, and 340 K). The simulation results showed that the free surface in the tip region of the strand has the most tendency to adhere to the printing platform heated at 340 K with the printing speed of 45 mm/s, as compared with other cases. This was affected by the lower dynamic viscosity in the region, relative to other cases, resulting from the high platform temperature and shear rate generated by the high printing speed.

Keywords: 3D printing; Computational Fluid Dynamics; Fused Filament Fabrication; thermo-fluid dynamics; polylactic acid.

Cite this as: Saldi, Z. S., Purnama, P., Nurmalia., Alfarisi, S., Arifin, M., & Suweco, A. M. 2025. Thermo-Fluid Dynamics of PLA Deposition in Fused Filament Fabrication 3D Printing: A Numerical Study. *IJAP: Indonesian Journal of Applied Physics, 15*(1), 110-123. doi: https://doi.org/10.13057/ijap.v15i1.87634

INTRODUCTION

The field of design and manufacturing has recently seen a widespread use of 3D printing, also known as additive manufacturing. This innovative technology has rapidly provided a new pathway for the prototyping and production of complex and customized objects, ranging from aerospace components [1-2], energy storage [3-4], to medical implants [5-6]. Among the various 3D printing techniques, Fused Filament Fabrication (FFF), also known as Fused Deposition Modeling (FDM), has gained popularity due to its simplicity, cost-effectiveness, and versatility [7]. FFF technique enables the layer-by-layer creation of objects by extruding a thermoplastic filament through a heated nozzle onto a build platform. The material is extruded in a controlled manner, creating a series of two-dimensional cross-sections stacked vertically to form a three-dimensional object. The versatility and accessibility of FFF makes it attractive for various applications, including rapid prototyping, customization, and low-volume production [8-10].

Polylactic Acid (PLA) is one of the most widely used thermoplastic filament materials in FFF 3D printing. PLA is derived from renewable resources such as cornstarch or sugarcane and is known for its biodegradability and biocompatibility [11]. These characteristics have contributed to PLA's popularity, especially in applications where sustainability and biocompatibility are essential. PLA exhibits a glass transition temperature around 60-65°C and melting temperature around 160-180°C [12], making it suitable for a wide range of applications, including medical devices, packaging prototypes, educational models, and figurines.

While FFF using PLA has proven its capabilities in producing functional prototypes and end-use parts, its potential is still far from fully explored. A critical aspect of 3D printing, often overlooked, is the thermo-fluid dynamics occurring during the deposition of successive layers of material. Previous study showed that the interlayer bond of PLA filaments in FFF 3D printing is often insufficient to promote a good mechanical strength [13]. Understanding and optimizing these dynamics is crucial for improving print quality, mechanical properties, and process reliability. In addition, insights into deposition thermo-fluid dynamics are also crucial when working with new filament materials, e.g., biopolymers [14].

The thermo-fluid dynamics in FFF refers to the intricate heat transfer and flow phenomenon that occur as successive layers of material are deposited during the 3D printing process. This includes three main aspects, i.e., heat transfer, material flow, and cooling/solidification. As each layer is deposited, it fuses with the previous one. Understanding how heat is transferred from the freshly extruded material to the previously deposited layer and how it dissipates within the printed object is important for controlling the printing process and optimizing interlayer bond, which affects material properties [15-17]. The flow behavior of the molten material as it exits the nozzle and spreads across the previous layer determines the final shape and quality of the printed part. Controlling material flow is essential for achieving precise geometries and minimizing defects. Rapid cooling and solidification of the deposited material are essential to maintain structural integrity and prevent deformation or warping [18]. Balancing the parameters that control these phenomena, for example printing speed and platform temperature, is thus a critical aspect of deposition thermo-fluid dynamics.

Numerical simulation plays a pivotal role in the understanding of interlayer thermo-fluid dynamics in FFF 3D printing. Traditional trial-and-error approaches of balancing the process parameters can be time-consuming and costly, making numerical modeling a cost-effective and efficient alternative. Through Computational Fluid Dynamics (CFD), one can simulate and analyze the interactions between heat transfer and material flows within the 3D printing process.

In view of the above motivation, this paper explores the numerical study of polymer deposition thermo-fluid dynamics in FFF 3D printing, with a specific focus on the use of PLA as the filament material. The long-term goal is to simulate the layer-by-layer deposition of the filament. However, in the current study, the scope is limited to a single layer deposition since the current objectives mainly lie in two aspects: (1) To develop a numerical model of the deposition thermo-fluid dynamics in FFF 3D printing; and (2) To investigate the influence of platform temperature and printing speed on the PLA strand thermo-fluid dynamics through CFD simulations based on the developed model. After these objectives have been met, extension of the model to simulate multiple layer deposition will follow.

METHOD

In this study, FFF 3D printing using PLA filament was evaluated using CFD simulations. The physical process is shown in Figure 1, which illustrates the typical FFF printing setup. The extruded filament flows through a nozzle with a diameter d_{noz} at a certain average flow rate Q_{noz} and temperature T_{noz}. Upon exiting the nozzle to ambient air with temperature T_{inf} , the filament is deposited on a heated platform bed (platform) at temperature T_b. The tip of the nozzle is elevated at a distance h_p from the platform surface. This distance is referred to as the print layer thickness. The nozzle makes a translating motion with respect to the platform, characterized by the printing speed U_p. These process parameters are summarized in Table 1.

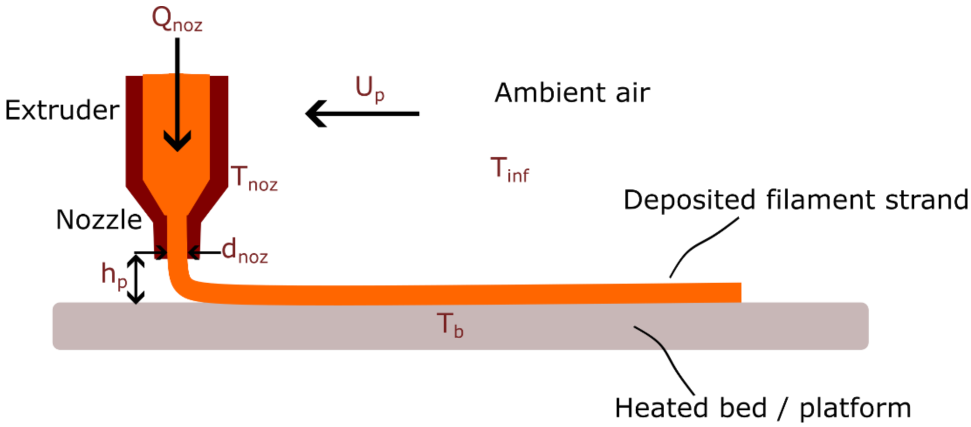

Figure 1. Illustration of a typical FFF 3D printing

Table 1. Process parameters used in the study

Parameters	Value	Unit
Ambient air temperature, T_{inf}	300	K
Nozzle diameter, d_{noz}	0.4	mm
Print layer thickness, h_p	0.4	mm
Nozzle/extruder temperature, T_{noz}	473	K
Average filament melt flow rate in the nozzle, Q_{noz}	5.03	mm^3/s
Printing speed, U_p	30; 45	mm^3/s
Bed/platform temperature, T_b	310; 320; 340	K

Numerical Model

Fluid flow and heat transfer phenomena during the deposition of filament in FFF 3D printing is governed by a set of conservation laws of continuum fluid, namely mass conservation (continuity), momentum conservation (Navier-Stokes), and energy conservation. These laws serve as the core of the numerical model to simulate the process, and they are expressed as follow, respectively:

$$\frac{\partial}{\partial t}(\rho) + \nabla \cdot (\rho \boldsymbol{U}) = 0 \tag{1}$$

$$\frac{\partial}{\partial t}(\rho \boldsymbol{U}) + \nabla \cdot (\rho \boldsymbol{U}\boldsymbol{U}) = -\nabla p + \nabla \cdot (\mu \nabla \boldsymbol{U}) + \boldsymbol{S}_S + \boldsymbol{S}_B \quad (2)$$

$$\frac{\partial}{\partial t}(\rho H) + \nabla \cdot (\rho \boldsymbol{U} H) = \nabla \cdot (k \nabla T) \quad (3)$$

In the above conservation equations, ρ is density, $\boldsymbol{U}$ velocity vector, p pressure, μ dynamic viscosity, H total enthalpy, k thermal conductivity, and T temperature.

The model also captures the PLA filament flow surrounded by gas phase (air) by employing the Eulerian framework of immiscible two-phase flows. The PLA filament as the primary phase was treated as non-Newtonian liquid. Air as the secondary phase was treated as Newtonian liquid. Both phases were assumed to be laminar and incompressible. In this framework, the Volume of Fluid (VoF) method was used, where both phases were represented by volume fraction α. The volume fraction of 1 refers to the PLA melt, whereas volume fraction of 0 refers to the surrounding air. The transport equation of the volume fraction is expressed as:

$$\frac{\partial}{\partial t}(\alpha) + \nabla \cdot (\boldsymbol{U}\alpha) = 0 \quad (4)$$

By solving the volume fraction transport, the dynamics of interface between the PLA melt and air can be captured, i.e., by reconstructing the computational cells having volume fraction between 0 and 1.

The momentum source terms $\boldsymbol{S}_S$ and $\boldsymbol{S}_B$ in Eq. (2) are due to surface force and buoyancy force, respectively. In the primary phase (PLA melt), the latter was neglected due to the small volume of the melt. On the contrary, buoyancy effect due to temperature gradients in the secondary (air) phase was accounted for in the simulation. This thermal buoyancy was formulated using the Boussinesq approximation.

Thermophysical Properties

The thermophysical properties of PLA filament and air are outlined in Table 2.

Table 2. Thermophysical properties of PLA filament and air used in the study

Properties	Value	Unit
PLA filament		
Density, ρ_{PLA}	1250	kg/m^3
Thermal conductivity, k_{PLA}	0.18	W/(m.K)
Specific heat capacity, $c_{p,\text{PLA}}$	2140	J/(kg.K)
Surface tension coefficient, σ	0.04	N/m
Air		
Reference density, $\rho_{0,\text{ air}}$	1.225	kg/m^3
Thermal conductivity, k_{air}	0.024	W/(m.K)
Specific heat capacity, $c_{p,\text{ air}}$	1006.43	J/(kg.K)
Dynamic viscosity, μ_{air}	1.79 x 10^{-5}	kg/(m.s)
Thermal expansion coefficient, β_{air}	0.0026	K^{-1}

Non-Newtonian Viscosity of PLA

Central to this study is the model to describe the PLA viscosity. As PLA exhibits shear-thinning behavior, it must be treated as non-Newtonian fluid [19]. Therefore, its viscosity should be modeled following the relation between shear stress and shear rate. Additionally, viscosity is also affected by non-isothermal condition and pressure, as found in the extrusion of PLA melt in FFF 3D printing, in which the temperature of filament and extruder is raised above the ambient temperature and there is a pressure build up in the narrow passage of the extruder before the filament melt exits the nozzle. In this work, the Cross-WLF rheology model was chosen to calculate the PLA viscosity [20-21], as it formulates comprehensively the viscosity variation based on shear rate, critical shear stress, and temperature. The PLA dynamic viscosity is expressed as follows:

$$\mu = \frac{\mu_0}{1+\left(\frac{\mu_0 \dot{\gamma}}{\tau^*}\right)^{1-n}} \tag{5}$$

where μ_0 is the zero-shear viscosity, or the constant viscosity as it approaches the limit of extremely low shear rates, $\dot{\gamma}$ the shear rate, τ^* critical shear stress at the transition to shear thinning, and n the power law index in the high shear rate regime. Both τ^* and n were obtained from curve fitting.

The zero-shear viscosity itself is a function of temperature, as follows:

$$\mu_0 = D_1 \exp\left(-\frac{A_1(T-T_g)}{A_2+(T-T_g)}\right) \tag{6}$$

where T_g is the reference temperature, taken as the glass transition temperature of PLA, and D_1, A_1, and A_2 are data-fitted coefficients. The rheological properties and coefficients are given in Table 3.

Table 3. Rheological properties and coefficients in the Cross-WLF viscosity model of PLA [20]

Properties and coefficients	Value	Unit
Critical shear stress, τ^*	1.29 x 10^5	N/m^2
Power law index, n	0.3826	-
Glass transition temperature, T_g	373	K
Coefficient, D_1	2.05 x 10^7	kg/(m.s)
Coefficient, A_1	16.71	-
Coefficient, A_2	51.6	K

Figure 2 shows the viscosity trend based on the variation of temperature and shear rates, according to Eq (5) and (6). Solidification of the melt as the temperature decreases can be represented by the increase of viscosity, which will effectively damp out the velocity field in the model when the viscosity becomes sufficiently high, according to the momentum conservation equation (Eq. (2)).

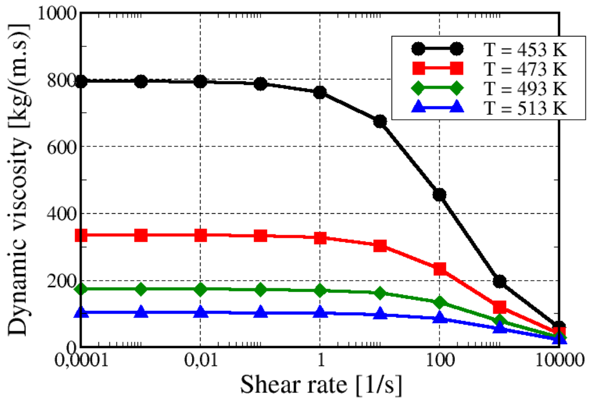

Figure 2. Viscosity variation with temperature and shear rates

Simulation Settings

The thermo-fluid dynamics of the PLA melt based on the numerical model outlined above was simulated using CFD software ANSYS Fluent 2020R2. As the Cross-WLF viscosity model was not readily available in the released version of the software, it was implemented into the software by programming the formula through User-defined Function (UDF).

The numerical simulations were performed on a computational domain in the Cartesian coordinate system, shown in Figure 3. The domain is bounded by the following boundaries: atmospheric (at top, left, right, and back), extruder inlet (at top of extruder), symmetry (at front), and platform wall (at bottom). The domain size in x, y, and z direction is 5 mm (from x = -1 to 4 mm) x 1 mm (from y = 0 to 1 mm) x 1 mm (from z = 0 to 1 mm), respectively. The nozzle was positioned such that its central axis is colinear with x = 0 mm. The atmospheric boundaries (at top, lateral side, and downstream the nozzle) were open and pressure outlet conditions were applied at these boundaries. At the PLA inlet, a Hagen-Poiseuille velocity profile was used. At the air inlet (upstream the nozzle), a constant velocity with the magnitude of print velocity was used. Symmetry boundary condition was imposed on the front plane (the central plane parallel to the path of the nozzle motion), as it was commonly found that the flow characteristic is symmetric with respect to this plane. This also gives the benefit of saving computational time. Along the platform wall, a constant temperature was imposed (as given in Table 4), and a constant contact angle of 80° for PLA was established. This value is within the range of PLA contact angle found in literature [22].

The translation motion of the nozzle during the printing process was not explicitly modeled in the simulation. Rather, the relative motion of the nozzle with respect to the platform was set by fixing the nozzle as stationary while imposing the printing velocity at the platform. At the nozzle wall, a constant uniform nozzle/extruder temperature and no-slip boundary conditions were applied. Initially, the internal cylindrical channel of the extruder was filled with PLA filament (volume fraction of 1) having temperature of T_{noz}.

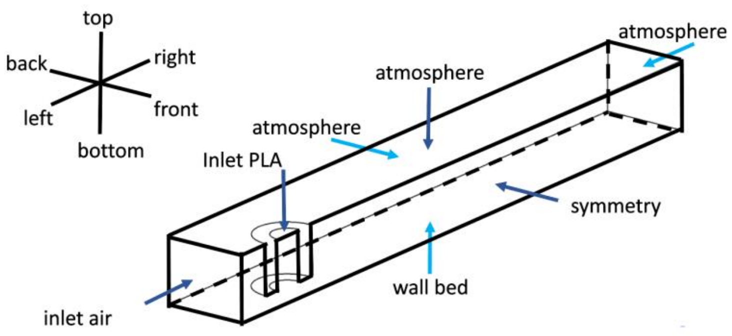

Figure 3. Computational domain (not to scale) and boundaries

The conservation equations in Ansys FLUENT were discretized using the finite volume method. The 2^{nd}-order upwind scheme was used to discretize the convective flux terms, whereas 1^{st}-order implicit Euler scheme was applied to the transient terms. Adaptive time stepping was employed, and an initial time step of 10^{-6} was applied for the first 100 time-marching iterations. The maximum global Courant number was set to 1. The under-relaxation factor of 0.3 was used for pressure and velocity vectors. A convergence criterion of 10^{-5} was used for the residual of linear equation matrix iteration to obtain velocity vectors, and 10^{-6} for energy, with a maximum number of iterations per time step set at 30. The pressure-velocity coupling was treated using the PISO algorithm.

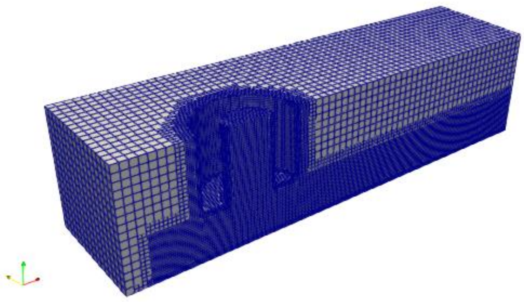

Figure 4. Computational mesh used in the simulations

The domain was spatially discretized into a finite number of hexahedral computational elements, with sufficiently fine elements allocated in the nozzle, the region of melt deposition, and the vicinity of walls, as shown in Figure 4. Based on the mesh sensitivity study, it was found that computational mesh of 450,000 elements offered a good trade-off between computational time and mesh-independence of the numerical solution. This mesh corresponds with the smallest computational element of the size 7.8 microns in all three directions. The mesh quality was also guaranteed by ensuring that the element aspect ratio in all three directions is close to 1 and non-orthogonality is sufficiently low. The simulations were performed using a computer running on Intel i7-9700K 3.60 GHz CPU with 6 core processors.

RESULTS AND DISCUSSION

The CFD simulations were performed for 6 cases, which represent a combination of 3 different platform temperatures (310, 320, and 340 K) and 2 printing speeds (30 and 45 mm/s). These values were selected because they are within the typical range used in FFF 3D printing. The platform temperature and printing speed were chosen as key variables because they significantly influence the thermo-fluid dynamics of polymer deposition in FFF 3D printing.

These parameters directly impact heat transfer and material flow of the deposition. The simulations are summarized in Table 4. The simulation time was set to 50 ms.

Table 4. Overview of the simulation case studies

Simulation case name	Printing speed [mm/s]	Platform temperature [K]
run_01	30	310
run_02	30	320
run_03	30	340
run_04	45	310
run_05	45	320
run_06	45	340

In the following subsections, the thermo-fluid dynamics of the PLA melt deposition will be discussed by evaluating the full-length and cross-sectional profiles of the deposited strand. The discussion will be based on evaluation of the relevant field variables computed in the CFD simulations, e.g., temperature, velocity, free surface profile, and dynamics viscosity.

Full-length Profiles of the Deposited Strand

Figure 5 shows the comparison of full-length profiles of the deposited strand at t = 50 ms in all 6 simulated cases, at the symmetry plane. The velocity vectors and free surface profile are shown. Inside the extruder, the PLA filament flows with a maximum velocity at its central axis, which is consistent with the Hagen-Poiseuille parabolic velocity profile for a flow in circular channel. As the filament touched the print platform, it was transported away downstream due to the imposed movement. The velocity vectors just above the platform represent the right level of imposed velocity, as compared with the listed values in Table 4. It is obvious that the cases with higher printing speed (run_04, 05, 06, at 45 mm/s) resulted in longer strand on the print platform than the other three cases (run_01, 02, 03, at 30 mm/s). The velocity difference also caused the free surface profile to differ between the two groups. Although all cases show similar profile qualitatively, i.e., the thickness of the strand is getting smaller when approaching the tip, for higher print speed (run_04, 05, 06) the stretching effect is higher, causing less steep top free surface than the ones with lower printing speed.

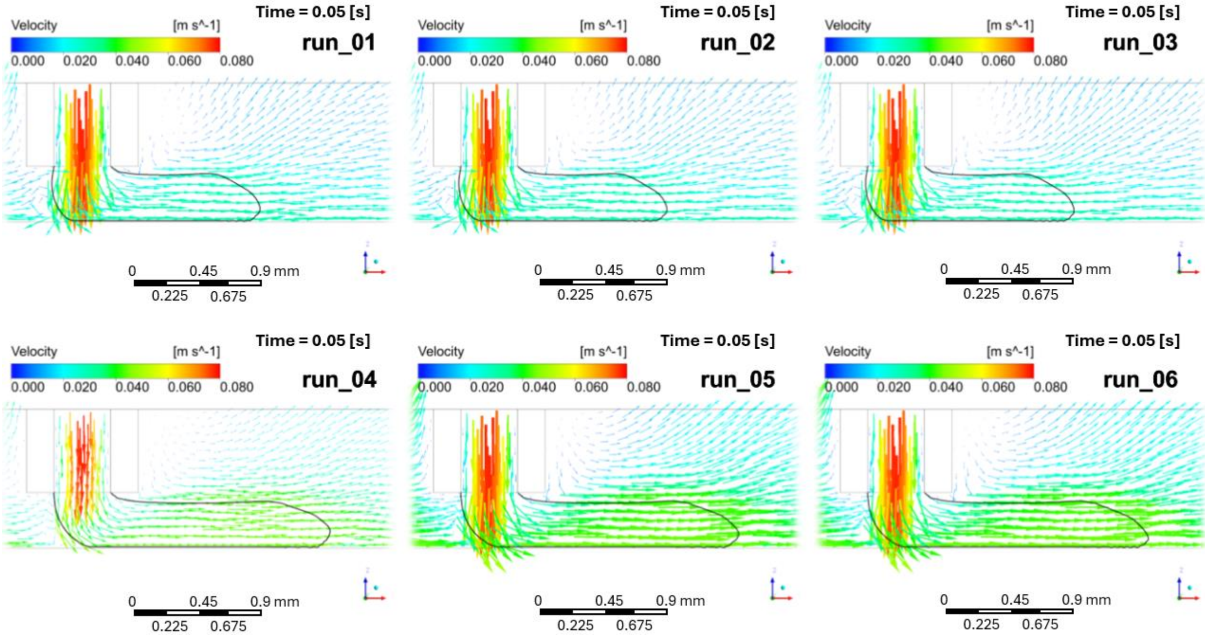

Figure 5. Velocity vectors and free surface profile on the symmetry plane at t = 50 ms

In terms of temperature distribution, all 6 cases show qualitatively similar tendencies, as shown in Figure 6. The filament in the nozzle and right below the nozzle exit reached temperatures equal to the nozzle/extruder temperature (T = 473 K), but away from the nozzle exit this temperature level was only maintained at the top surface of the strand. There was cooling effect on the platform due to its lower temperature than the nozzle. It is also clear that the cooling region has the largest thickness at the tip of the strand, i.e., at the furthest point from the nozzle exit.

Figure 7 shows the comparison between the temperature distribution taken at two sample lines at the symmetry plane. The first line was taken close to the platform (z = 0.1 mm), whereas the second close to the top surface of the strand (z = 0.3 mm). The temperature gradient in the x direction close to the platform (Figure 7a and 7c) was higher than that close to the top surface (Figure 7b and 7d), regardless of the printing speed. In the former, the temperature drop can be immediately observed as the distance from the nozzle increases, whereas in the latter the temperature was relatively constant up to around x = 1.2 mm in the 30 mm/s cases and x = 1.5 mm in the 45 mm/s cases. This is likely to be caused by the cooling effect from the platform, which has lower temperature than the extruded PLA strand from the nozzle.

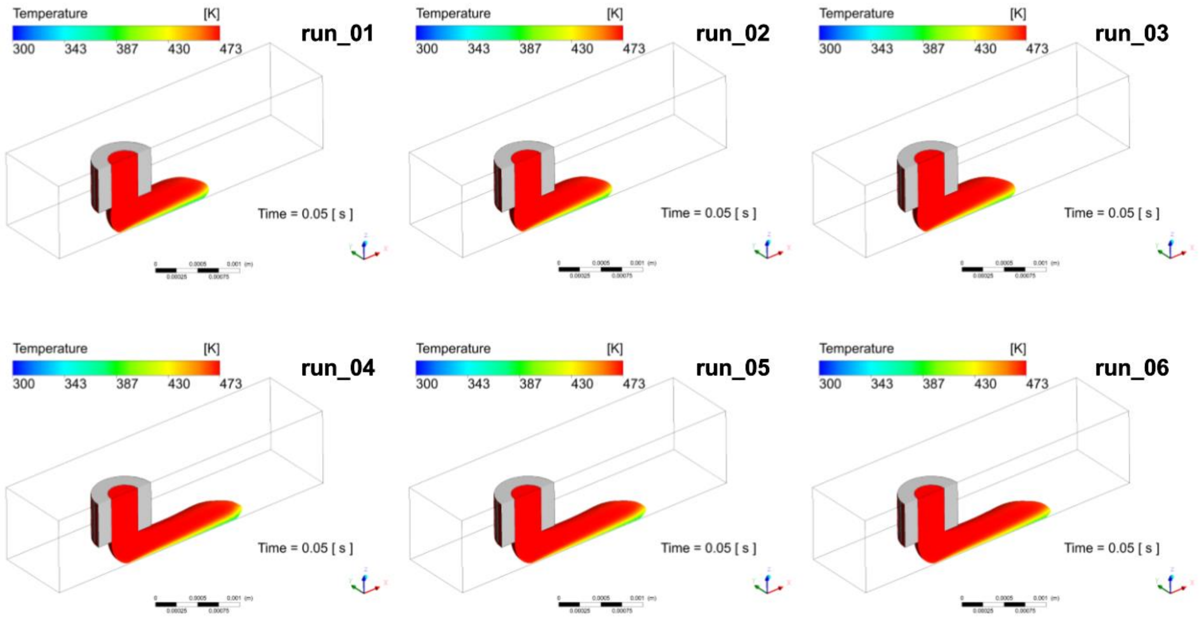

Figure 6. Temperature fields of the strand at t = 50 ms

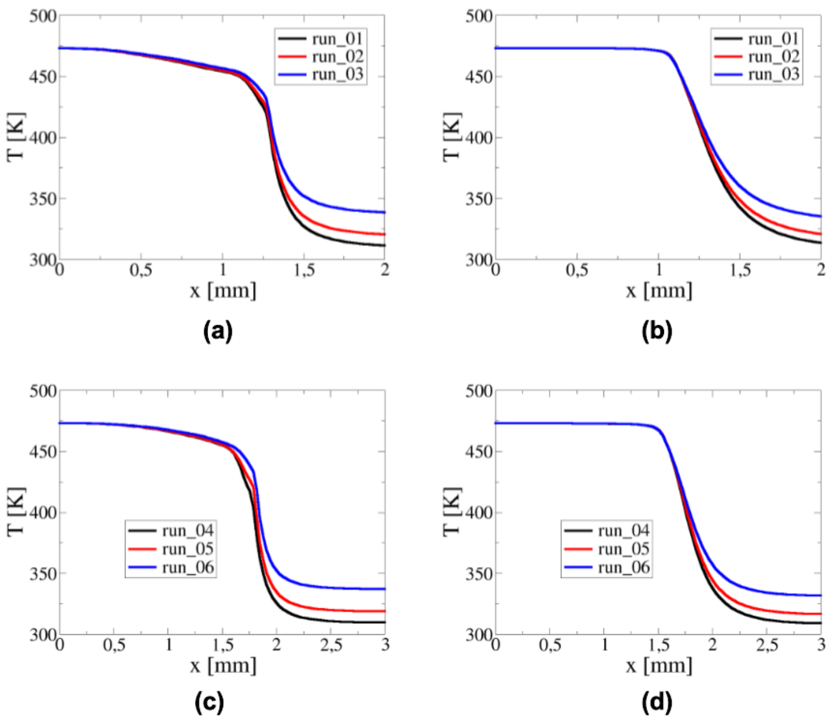

Figure 7. Comparison of temperature distribution at the symmetry plane at t = 50 ms. Top: run_01, 02, 03 at (a) z = 0.1 mm; (b) z = 0.3 mm; Bottom: run_04, 05, 06 at (c) z = 0.1 mm; (d) z = 0.3 mm

Figure 8 shows the comparison of dynamic viscosity fields among all cases. As this property was set as a function of temperature (according to Eq. (5) and (6)), its distribution followed the distribution of temperature fields in Figure 6. However, an inverse relation applied, where the region of high temperature had low dynamic viscosity. In the regions of low temperature above the platform, the viscosity was higher. At the tip of the strand with low temperature, the dynamic viscosity increased exponentially, as implied by the Cross-WLF viscosity model in Eq. (6).

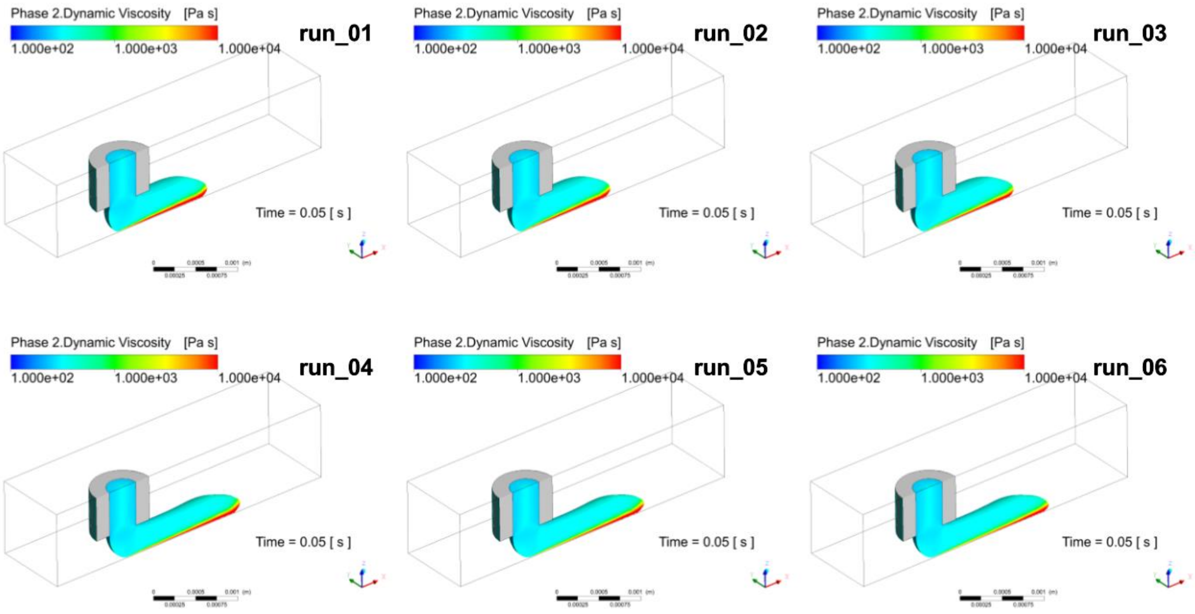

Figure 8. Dynamic viscosity fields of the strand at t = 50 ms

Cross-sectional Profiles of the Deposited Strand

In addition to the full-length profile discussed in the previous subsection, the cross-sectional profiles of the deposited strand were also extracted from the simulations. Comparison of the free surface profiles in the cross-sections can capture the effect of the varying parameters on the deposited strand characteristics.

Figure 9 shows the comparison of free surface topology at three cross sections (y-z planes) in the print direction (x direction), representing the region near the nozzle, middle region, and further from the nozzle (tip of the strand), respectively. As there were two printing speeds, the cross-section locations also differ between the low speed (top figures) and the higher speed (bottom figures). Accordingly, the topology was evaluated separately between them. Figures 9a, 9b, and 9c correspond to the cross-section comparison between run_01, 02, and 03 (printing speed of 30 mm/s) at x = 0.5, 0.8, and 1.2 mm, respectively. Figures 9d, 9e, and 9f represent the cross-section comparison between run_04, 05, and 06 (printing speed of 45 mm/s) at x = 0.75, 1.2, and 1.7 mm, respectively. At the cross section nearest to the nozzle, the free surface profiles among the cases with the same printing speed are perfectly identical. At the middle cross sections, free surface topology in the cases of 30 mm/s printing speed still looks identical, but a small deviation occurred in 45 mm/s cases at the lateral side of the strand (around y = 0.28 mm). As the cross section moves further downstream towards the strand tip, the difference in free surface profile became more pronounced with 45 mm/s speed, whereas with 30 mm/s the difference is smaller, but more obvious than in the middle cross section. At the cross section close to the tip, the free surface at the bottom corner in the cases with the highest platform temperature (run_03 and run_06, at 340 K) tend to get closer to the platform, as compared with other cases with lower platform temperature.

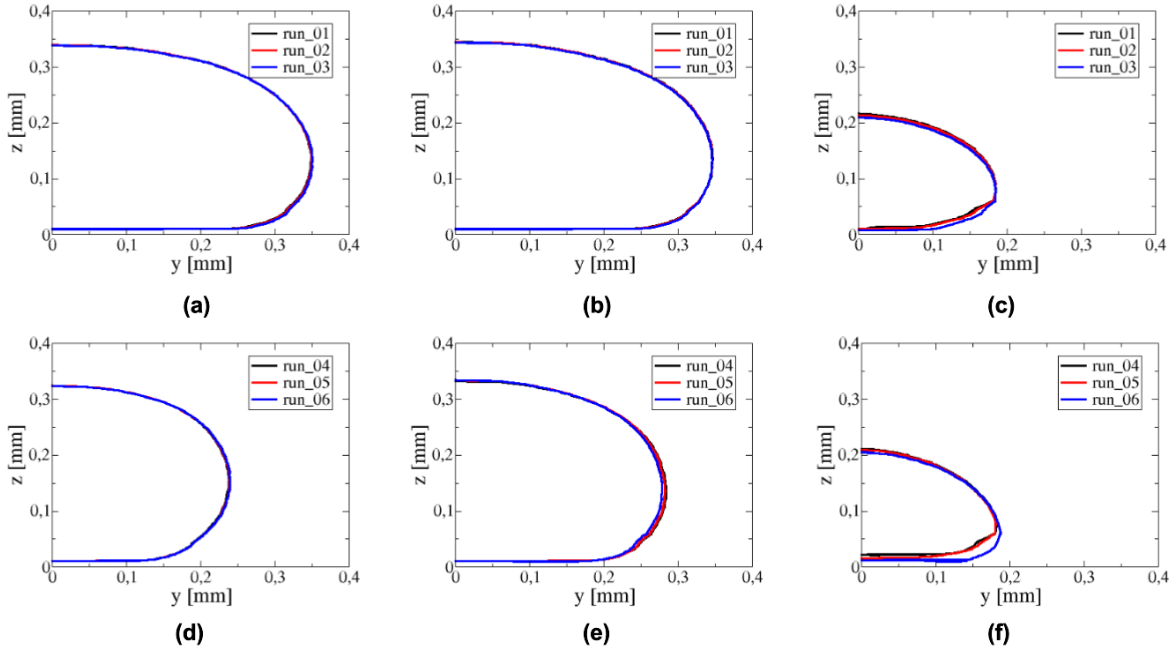

Figure 9. Comparison of free surface topology at the Y-Z cross sections at t = 50 ms. Top: run_01, 02, 03 at (a) x = 0.5 mm; (b) x = 0.8 mm; and (c) x = 1.2 mm; Bottom: run_04, 05, 06 at (d) x = 0.75 mm; (e) x = 1.2 mm; and (f) x = 1.7 mm.

Explanation of the mechanism causing the tendency of free surface at the strand edge near the tip to stick to the platform at high platform temperature could be based on the interplay between surface tension, viscosity, and shear rates. Surface tension generally decreases with temperature, preventing the free surface from minimizing its surface area. However, in the current simulation surface tension was assumed to be independent of temperature (Table 2). Therefore, it is important to look at the relation between viscosity and temperature. At high temperature, the dynamic viscosity decreases, which makes the PLA surface flow more easily. Moreover, shear rates also affect dynamic viscosity. With higher printing speed, the deposited strand experiences higher shear rates at the region close to the platform surface. As indicated in Eq (5) and (6) as well as Figure 2, the PLA dynamic viscosity decreases with shear rates, leading to higher tendency of the free surface to collapse when the platform temperature is the highest (Figure 9f).

The above analysis highlights that combination of printing speed and platform temperature determines the thermos-fluid dynamics of the deposited PLA strand, which also includes the free surface characteristics. It must be underlined, though, that further improvement of the model and simulation is needed. For example, temperature-dependent surface tension and contact angle can be implemented in future study to capture more physical representation of the PLA deposition. Experimental measurements are also required to better validate and understand the deposition behavior.

CONCLUSION

This paper presents the thermo-fluid dynamics of Polylactic Acid (PLA) strand during Fused Filament Fabrication (FFF) 3D printing using Computational Fluid Dynamics (CFD) simulations. Focusing on strand deposition on the printing platform, the study explored six printing cases with variations in key parameters: printing speed (30 and 45 mm/s) and platform temperature (310, 320, and 340 K). The simulations revealed that higher printing speed and elevated platform temperature resulted in longer strands with unique free surface profiles at the tip region. Cross-sectional profiles provided additional insights, demonstrating identical free surface profiles among cases with the same printing speed near the nozzle. Deviations occurred at middle cross-sections for higher printing speeds, which became more pronounced towards the strand tip. At the tip, high platform temperatures notably led to the free surface at the strand edge sticking closer to the platform, influenced by the interplay of temperature, viscosity, and shear rates. The dynamic viscosity decreased with higher temperature and shear rates, contributing to the collapse tendency of the free surface. The numerical study captured the interactions governing PLA deposition in FFF 3D printing. The influence of key parameters, specifically printing speed and platform temperature, on strand characteristics and free surface profiles was examined. The findings emphasize the relations between temperature, viscosity, and shear rates, which provided the mechanisms driving the observed trends. The numerical model and simulation potentially contribute to optimizing 3D printing processes for high-quality prints. Understanding the thermo-fluid dynamics aids in tailoring process parameters, with implications for material flow, layer adhesion, and overall print quality. This will also allow for exploration into broader applications and development of FFF printing materials, driving innovation in additive manufacturing technologies.

ACKNOWLEDGMENTS

The authors would like to thank DRTPM (Directorate of Research, Technology and Community Service), The Ministry of Education, Culture, Research and Technology (Kemendikbudristek) for the research grant support (contract number 179/E5/PG.02.00.PL/2023).

REFERENCES

1 Najmon, J. C., Raeisi, S. & Tovar, A. 2019. *Review of Additive Manufacturing Technologies and Applications in the Aerospace Industry*. Additive Manufacturing for the Aerospace Industry. Elsevier.

2 Blakey-Milner, B., Gradl, P., Snedden, G., Brooks, M., Pitot, J., Lopez, E., Leary, M., Berto, F. & Du Plessis, A. 2021. Metal Additive Manufacturing in Aerospace: A Review. *Mater Des, 209*, 110008.

3 Zhang, F., Wei, M., Viswanathan, V.V., Swart, B., Shao, Y., Wu, G. & Zhou, C. 2017. 3D Printing Technologies for Electrochemical Energy Storage. *Nano Energy*, *40*, 418–431.

4 Zhu, C., Liu, T., Qian, F., Chen, W., Chandrasekaran, S., Yao, B., Song, Y., Duoss, E.B., Kuntz, J.D., Spadaccini, C.M. & Worsley, M.A. 2017. 3D Printed Functional Nanomaterials for Electrochemical Energy Storage. *Nano Today, 15*, 107–120.

5 Popov, V.V., Muller-Kamskii, G., Kovalevsky, A., Dzhenzhera, G., Strokin, E., Kolomiets, A. & Ramon, J. 2018. Design and 3D-printing of Titanium Bone Implants: Brief Review of Approach and Clinical Cases. *Biomed Eng Lett*, *8*, 337–344.

6 Tan, G., Ioannou, N., Mathew, E., Tagalakis, A.D., Lamprou, D.A. & Yu-Wai-Man, C. 2022. 3D Printing in Ophthalmology: From Medical Implants to Personalised Medicine. *Int J Pharm, 625*, 122094.

7 Haryńska, A., Carayon, I., Kosmela, P., Szeliski, K., Łapiński, M., Pokrywczyńska, M., Kucińska-Lipka, J. & Janik, H. 2020. A Comprehensive Evaluation of Flexible FDM/FFF 3D Printing Filament as a Potential Material in Medical Application. *Eur Polym J, 138*, 109958.

8 Rayna, T. & Striukova, L. 2016. From Rapid Prototyping to Home Fabrication: How 3D Printing is Changing Business Model Innovation. *Technol Forecast Soc Change, 102*, 214–224.

9 Shi, H., Cao, J., Sun, Z., Ghazi, Z.A., Zhu, X., Han, S., Ren, D., Lu, G., Lan, H. & Li, F. 2023. 3D Printing Enables Customizable Batteries. *Batteries Supercaps, 6*, e202300161.

10 Gebler, M., Uiterkamp, A.S. & Visser, C. 2014. A Global Sustainability Perspective on 3D Printing Technologies. *Energy Policy, 74*, 158–167.

11 Chen, X., Chen, G., Wang, G., Zhu, P. & Gao, C. 2020. Recent Progress on 3D-printed Polylactic acid and its Applications in Bone Repair. *Adv Eng Mater*, *22*, 1901065.

12 Murariu, M. & Dubois, P. 2016. PLA Composites: From Production to Properties. *Adv Drug Deliv Rev*, *107*, 17–46.

13 Srinivas, V., van Hooy-Corstjens, C.S., Rastogi, S. & Harings, J.A. 2020. Promotion of Molecular Diffusion and/or Crystallization in Fused Deposition Modeled Poly (lactide) Welds. *Polymer*, *202*, 122637

14 Chaunier, L., Guessasma, S., Belhabib, S., Della Valle, G., Lourdin, D. & Leroy, E. 2018. Material Extrusion of Plant Biopolymers: Opportunities & Challenges for 3D Printing. *Addit Manuf, 21*, 220–233.

15 Lepoivre, A., Boyard, N., Levy, A. & Sobotka, V. 2020. Heat Transfer and Adhesion Study for the FFF Additive Manufacturing Process. *Procedia Manuf*, *47*, 948–955.

16 Comminal, R., Serdeczny, M.P., Pedersen, D.B. & Spangenberg, J. 2018. Numerical Modeling of the Strand Deposition Flow in Extrusion-based Additive Manufacturing. *Addit Manuf*, *20*, 68–76.

17 Ufodike, C.O. & Nzebuka, G.C. 2022. Investigation of Thermal Evolution and Fluid Flow in the Hot-End of a Material Extrusion 3D Printer using Melting Model. *Addit Manuf*, *49*, 102502.

18 Salentijn, G.I., Oomen, P.E., Grajewski, M. & Verpoorte, E. 2017. Fused Deposition Modeling 3D Printing for (Bio) Analytical Device Fabrication: Procedures, Materials, and Applications. *Anal Chem*, *89(13)*, 7053–7061.

19 Quintana, J.L.C., Hiemer, S., Duarte, N.G. & Osswald, T. 2021. Implementation of Shear Thinning Behavior in the Fused Filament Fabrication Melting Model: Analytical Solution and Experimental Validation. *Addit Manuf*, *37*, 101687.

20 Mishra, A.A., Momin, A., Strano, M. & Rane, K. 2022. Implementation of Viscosity and Density Models for Improved Numerical Analysis of Melt Flow Dynamics in the Nozzle during Extrusion-based Additive Manufacturing. *Prog Addit Manuf*, *7*, 1–14.

21 Kim, S.K. & Kazmer, D.O. 2022. Non-isothermal non-Newtonian Three-dimensional Flow Simulation of Fused Filament Fabrication. *Addit Manuf*, *55*, 102833.

22 Tümer, E.H. & Erbil, H.Y. 2021. Extrusion-based 3D Printing Applications of PLA Composites: A Review. *Coatings*, *11*, 390.